Impact of the synthesis parameters on the solid state properties and the CO oxidation performance of ceria nanoparticles

Maria Lykaki,[a] Eleni Pachatouridou,[ab] Eleni Iliopoulou,[b] Sónia A. C. Carabineiro[c] and Michalis Konsolakis*[a]

Ceria-based materials have received considerable attention in catalysis field due to their unique physicochemical characteristics. Compared to bulk ceria, nanosized ceria received particular interest, due to its high surface to volume ratio, improved reducibility and optimal morphological features. Hence, the fine-tuning of ceria properties by means of advanced synthesis routes is of particular importance. In this regard, the present work aims at investigating the impact of synthesis parameters on the solid state properties of CeO_2 materials. Four different time- and cost-effective preparation methods were followed, i.e. thermal decomposition, co-precipitation and hydrothermal method of low and high NaOH concentration, employing in all cases $Ce(NO_3)_3 \cdot 6H_2O$ as cerium precursor. A complementary characterization study, involving N_2 adsorption at $-196\ ^\circ C$ (BET method), X-ray diffraction (XRD), X-ray photoelectron spectroscopy (XPS), H_2 temperature-programmed reduction (H_2-TPR) and scanning/ transmission electron microscopy (SEM/TEM), was carried out to gain insight into the impact of synthesis route on the textural, structural, morphological and redox properties. The results revealed the superiority of the hydrothermal method towards the development of ceria nanoparticles of high specific surface area ($>90\ m^2\ g^{-1}$), well-defined geometry (nanorods) and improved redox properties. CO oxidation was employed as a probe reaction to gain insight into the structure–activity correlation. Ceria nanorods prepared by hydrothermal method of high NaOH concentration demonstrated the optimum CO oxidation performance. A direct quantitative correlation between the catalytic activity and the abundance of easily reduced, loosely bound oxygen species, was revealed. Hence, this particular reactivity descriptor can potentially be used for the rational design of ceria-based materials.

Introduction

Cerium oxide (CeO_2) or ceria has lately received considerable attention as catalyst or supporting carrier in numerous catalytic processes,[1–3] involving among others the oxidation of CO, the reduction of NO_x, water–gas shift reaction, reforming reactions and soot combustion, as well as in further applications like optics,[4] biotechnology[5] and so on. The wide application range of ceria-based materials is largely due to the unique properties of ceria, like high thermal stability, high oxygen storage capacity (OSC) and oxygen mobility.[1–3,6–8] The facile switch between the two oxidation states (Ce^{3+}/Ce^{4+}) accompanied by the formation

of surface defects, such as oxygen vacancies, is considered responsible for its enhanced redox properties.[1–3,9–12]

Moreover, in the nanoscale, materials exhibit important features due to their quantum size effects. The surface area is substantially increased by decreasing particle size to the nanometer scale. These nanomaterials show abundance in defect sites such as oxygen vacancies and have more surface atoms than their bulk counterparts.[1–3,13–16]

Numerous methods have been employed for the synthesis of nano-sized ceria particles, such as hydrothermal,[17,18] sonochemical,[19] reverse micelles[20] etc., while precipitation method is considered as one of the most widely employed methods due to its simplicity and low cost.

The preparation method affects enormously the morphological and surface characteristics of CeO_2, leading to various geometries, such as nanorods, nanocubes, nanowires, etc.[21,22] In addition, the variation of several parameters during the synthesis procedure (i.e., temperature and base concentration) can lead not only to different ceria morphologies with high shape purity, but also to structures with tunable surface areas and defect concentrations.[23–26]

[a]School of Production Engineering and Management, Technical University of Crete, GR-73100 Chania, Crete, Greece. E-mail: mkonsol@science.tuc.gr; Web: http://www.tuc.gr/konsolakis.html; Tel: +30 28210 37682

[b]Chemical Process & Energy Resources Institute (CPERI), Centre for Research & Technology Hellas (CERTH), 6th km. Charilaou–Thermi Rd., P.O. Box 60361, GR-57001, Thessaloniki, Greece

[c]Laboratório de Catálise e Materiais (LCM), Laboratório Associado LSRE-LCM, Faculdade de Engenharia, Universidade do Porto, 4200-465 Porto, Portugal

For instance, Liu *et al.*[27] synthesized CeO_2 samples by precipitation, hydrothermal and citrate sol–gel methods. CeO_2 prepared with hydrothermal method showed larger surface area, average pore diameter and pore volume. Makinose *et al.*[28] fabricated ceria nanoparticles (NPs) with controlled crystal orientations *via* an oleate-modified hydtrothermal method; by altering the molar ratio of oleate to cerium ions in the reaction solution different ceria facetes were obtained.

CO oxidation reaction has been widely employed as a probe reaction to gain insight into the structure–activity correlations.[6,10,12,21,26,29–31] It is generally believed that CO oxidation over ceria proceeds *via* a Mars-van Krevelen mechanism which involves the removal of surface lattice oxygen by CO and the consequent annihilation of oxygen vacancies by gas phase oxygen.[30] Besides the importance of surface oxygen defects, the morphology and the crystallite size are also believed to affect the catalytic efficiency.[21,26,29–31] Piumetti *et al.*[21] have found that among a series of hydrothermally prepared ceria samples, ceria-nanocubes demonstrated the best CO oxidation performance. In a similar manner, the enhanced CO oxidation activity of ceria nanocubes, in comparison to conventional morphologies was verified by Vilé *et al.*[31], and attributed to the different oxygen vacancy chemistry of exposed facets.

Theoretical[32,33] and experimental[30,31,34] studies have shown that anionic vacancies energy formation is strongly dependent on exposed facets, following the order {111} > {100} > {110}. Hence, particular attention has been devoted on the synthesis of ceria with a high number of active crystal planes. In this regard, Piumetti *et al.*[35] showed that ceria nanocubes exhibited the best catalytic performance for the soot combustion due to the abundance of highly reactive {100} and {110} surfaces. Aneggi *et al.*[34] also showed, by comparing ceria samples of similar surface area, that a higher soot oxidation activity can be obtained for nanocubes and nanorods as compared to polycrystalline samples.

Despite the numerous studies in the field there is still a lack of understanding in relation to the impact of surface (*e.g.*, oxygen defects, exposed facets, surface area) and bulk (*e.g.*, crystallite size) properties on the catalytic activity. The present work aims at comparatively explore the impact of various widely employed synthesis methods, *i.e.* precipitation, thermal decomposition and hydrothermal, on the solid state properties of ceria samples. Particular emphasis is given on the synthesis parameters in order the preparation methods to be cost-effective and not time-consuming. Various characterization techniques (BET, XRD, H_2-TPR, SEM/TEM and XPS) were used in order to assess the impact of each preparation method on the structural, morphological and redox properties. Moreover, CO oxidation reaction was employed as probe reaction to gain insight into structure–activity correlation. Interestingly, a linear quantitative correlation between the CO oxidation activity and the amount of surface-capping oxygen of ceria is revealed. No particular correlation was found between the textural/structural characteristics and the catalytic performance.

Experimental

Materials synthesis

All of the chemicals used in this work were of analytical reagent grade. $Ce(NO_3)_3 \cdot 6H_2O$ (purity ≥99.0%, Fluka) was used as precursor for the preparation of ceria materials. NH_3 (25% v/v, EMSURE), NaOH (purity ≥98%, Sigma-Aldrich) and ethanol (purity 99.8%, ACROS) were also employed during synthesis procedure.

Different nanostructured ceria composites were synthesized by various methods, namely: thermal decomposition, precipitation method, and hydrothermal method. For the preparation of ceria by thermal decomposition (CeO_2-D) the $Ce(NO_3)_3 \cdot 6H_2O$ precursor was heated at 500 °C for 2 h under air flow. Ceria by precipitation (CeO_2-P) was prepared as follows: $Ce(NO_3)_3 \cdot 6H_2O$ was initially dissolved in double deionized water (0.50 M) until complete dissolution of the precursor compound. Ammonia solution (25% v/v) was then added at room temperature to the continuously stirred solution until pH reached the value of 9–10, and kept stable for 3 h. The resulting solution was filtered under vacuum and a gel was formed. The precipitate was dried overnight at 110 °C for 12 h and calcined at 500 °C for 2 h under air flow (heating ramp 5 °C min^{-1}).

Two ceria samples were prepared by the hydrothermal method employing low (CeO_2-HL) and high (CeO_2-HH) NaOH concentration. For the synthesis of CeO_2-HL, 0.45 mol NaOH was initially dissolved in 75 mL of double deionized water. Then, 175 mL of aqueous solution containing 23 mmol $Ce(NO_3)_3 \cdot 6H_2O$ (0.13 M) was added in the above solution under vigorous stirring until the formation of a milky slurry. The mixture was left for additional stirring for 1 h. The final slurry was then transferred into a 1 L Teflon bottle and aged at 90 °C for 24 h. Afterwards, the bottle was cooled to room temperature before the solid products were recovered by centrifugation. The materials were washed thoroughly with double deionized water until pH 7 to remove any co-precipitated salts and then washed with ethanol to avoid hard agglomeration in the nanoparticles. The precipitate was dried overnight at 90 °C for 12 h, followed by calcination at 500 °C for 2 h under air flow (heating ramp 5 °C min^{-1}). To obtain the CeO_2-HH sample, the same procedure was followed as above with only one variation: 2.75 mol NaOH instead of 0.45 mol was utilized.

Materials characterization

The textural characteristics of the as prepared catalysts were determined by the N_2 adsorption–desorption isotherms at −196 °C (Nova 2200e Quantachrome flow apparatus). Specific surface areas (m^2 g^{-1}) were obtained according to the Brunauer–Emmett–Teller (BET) method at relative pressures in the 0.05–0.30 range. The specific pore volume (cm^3 g^{-1}) was calculated based on the highest relative pressure, whereas the average pore size diameter (dp, nm) was determined by the Barrett–Joyner–Halenda (BJH) method. Prior to measurements the samples were degassed at 250 °C for 5 h under vacuum.

The crystalline structure of ceria sample was determined by powder X-ray diffraction (XRD) on a Siemens D 500

diffractometer operated at 40 kV and 30 mA with Cu Kα radiation ($\lambda = 0.154$ nm). Diffractograms were recorded in the 2–80° 2θ range and at a scanning rate of 0.02° s^{-1}. The Scherrer eqn (1) was employed to determine the primary particle size of a given crystal phase based on the most intense diffraction peak of CeO_2 patterns (2θ: 28.5° and 47.6°).

$$D_{XRD} = \frac{K\lambda}{\beta \cos \theta} \qquad (1)$$

where K is the Scherrer constant; λ is the wavelength of the X-ray in nm; β is the line broadening; θ is the Bragg angle.[36]

Temperature Programmed Reduction (H_2-TPR) experiments were carried out in a fully automated AMI-200 Catalyst Characterization Instrument (Altamira Instruments) under H_2 atmosphere, to acquire information on the reducibility of the samples. In a typical TPR experiment, ~50 mg of sample was placed in a U-shaped quartz tube, located inside an electrical furnace, and heated up to 1100 °C at 10 °C min^{-1} under He flow of 29 cm^3 min^{-1} and H_2 flow of 1.5 cm^3 min^{-1}. The H_2 consumption was calculated by the integrated area of TPR peaks, calibrated against a known amount of CuO standard sample.[37,38]

Morphological characterization was carried out by scanning electron microscopy (SEM), using a FEI Quanta 400 FEG ESEM (15 keV) electron microscope. The sample powders were mounted on double sided adhesive tape and observed at different magnifications under two different detection modes: secondary and backscattered electrons. Energy-dispersive X-ray spectroscopy (EDS) confirmed the nature of the components.

Transmission electron microscopy (TEM) analyses were performed on a Leo 906 E apparatus, at 100 kV. Samples were prepared by ultrasonic dispersion in ethanol and placed on a copper grid for analysis.

X-ray photoelectron spectroscopy (XPS) analyses were performed on a VG Scientific ESCALAB 200A spectrometer using Al Kα radiation (1486.6 eV). The charge effect was corrected taking the C 1s peak as a reference (binding energy of 285 eV). CASAXPS software was used for data analysis.

Catalytic activity studies

Catalytic tests for CO oxidation were carried out in a quartz fixed-bed reactor (9 mm i.d.). The catalyst (400 mg) and a layer of quartz wool were filled in the reactor. The total flow rate of the feed gas (2000 ppm CO and 1 vol% O_2 in He) was 500 cm^3 min^{-1}, corresponding to a Gas Hour Space Velocity (GHSV) of

39 000 h^{-1}. Catalytic evaluation measurements were carried out by increasing the temperature by 25-degree steps up to 500 °C. The reactant CO was analyzed by using an online CO analyzer (Horiba VIA-510). The CO conversion (X_{CO}, %) was calculated by the following equation:

$$X_{CO}(\%) = \frac{[CO]_{in} - [CO]_{out}}{[CO]_{in}} \times 100 \qquad (2)$$

where $[CO]_{in}$ and $[CO]_{out}$ are the CO concentration (ppm) in the inlet and outlet gas streams, respectively.

Kinetic measurements were also carried out under differential conditions (at temperatures lower than ca. 300 °C) to gain insight into the intrinsic activity of ceria samples. The specific reaction rate of CO consumption (r_{CO}, nmol m^{-2} s^{-1}) was calculated using the eqn (3), whereas the Arrhenius plot was used to determine the activation energy (E_a, kJ mol^{-1}) and the pre-exponential factor (A, nmol m^{-2} s^{-1}).

$$r_{CO} = \frac{X_{CO} \times [CO]_{in} \times F}{100 \times 60 \times V_m \times m_{cat} \times S_{BET}} \times 10^9 \qquad (3)$$

where F (cm^3 min^{-1}) is the total flow rate, V_m (cm^3 mol^{-1}) is the gas molar volume at STP conditions (298 K and 1 bar), m_{cat} (g) is the mass of catalyst and S_{BET} (m^2 g^{-1}) is the surface area.

Results and discussion

Textural and structural characterization (BET, XRD)

The main textural properties of ceria materials (BET surface area, total pore volume, average pore size diameter) are presented in Table 1. The average grain size, D_{BET}, was also calculated using the following eqn (4), on the assumption of the particle sphericity.

$$D_{BET} = \frac{6 \times 1000}{S \times d} \qquad (4)$$

where S is the BET surface area (m^2 g^{-1}) and d is the density of ceria in the fluorite structure (7.215 g cm^{-3}).[39]

It is evident that the ceria samples prepared by the hydrothermal method exhibit the optimum textural characteristics followed by thermal decomposition and precipitation. In particular, the sample prepared by the hydrothermal method of low NaOH concentration (CeO_2-HL) possesses the highest BET area (109.4 m^2 g^{-1}), followed by CeO_2-HH (91.8 m^2 g^{-1}), CeO_2-D (87.2 m^2 g^{-1}) and CeO_2-P (53.2 m^2 g^{-1}). These findings clearly revealed the pronounced impact of hydrothermal synthesis on

Table 1 Textural/structural characteristics of ceria samples

Sample	BET surface area (m^2 g^{-1})	Pore volume (cm^3 g^{-1})	Average pore size (nm)	Average grain size, D_{BET}^a (nm)	Average crystallite diameter, D_{XRD}^b (nm)	ψ (D_{BET}/D_{XRD})
CeO_2-P	53.2	0.087	6.6	15.6	15.2	1.03
CeO_2-D	87.2	0.25	11.6	9.5	9.3	1.02
CeO_2-HH	91.8	0.71	30.9	9.1	13.2	0.69
CeO_2-HL	109.4	1.04	38.1	7.6	9.5	0.80

^{a} Calculated applying eqn (4). ^{b} Calculated applying Scherrer eqn (1).
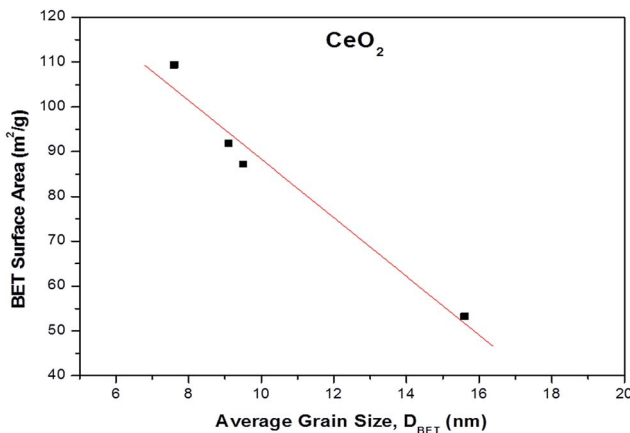
Fig. 1 BET surface area ($m^2 g^{-1}$) as a function of average grain size (nm) for the different CeO_2 samples.

the textural characteristics, as will be further discussed in the sequence.

The results of BET surface area as a function of average grain size (nm) for the different ceria samples are depicted in Fig. 1. It is evident that the BET surface area is inverse function of average grain size, implying that the surface area of ceria samples increase with decreasing grain size.[40]

To gain insight into the agglomeration extent of the primary crystallites, the factor $\psi = D_{BET}/D_{XRD}$ was also calculated (Table 1).[41] Ceria samples prepared by precipitation and thermal decomposition (CeO_2-P and CeO_2-D, respectively) exhibit a similar ψ value of *ca.* 1.0, implying no degree of aggregation. However, the crystallite size is larger than D_{BET} for CeO_2-HH and CeO_2-HL, resulting in ψ values lower than 1.0 (0.69 and 0.80, respectively). The latter indicates non-spherical particles with a small degree of aggregation.[42] Therefore, the assumption of the particle sphericity for the calculation of D_{BET} may not apply to the samples prepared by the hydrothermal method. This finding is in accordance with the TEM analysis (*vide infra*), which indicates the formation of NPs of specific shape (*e.g.*, nanorods) in CeO_2 samples prepared by the hydrothermal method.

Fig. 2a shows the pore size distribution (PSD) of as-prepared samples. A maxima at pore diameters higher than 3 nm is obtained in all cases, implying the presence of mesopores.[43] The CeO_2-HL sample possesses the highest average pore size (38.1 nm), followed by CeO_2-HH (30.9 nm), CeO_2-D (11.6 nm) and CeO_2-P (6.6 nm). The highest pore volume is observed at 8.14, 3.52, 7.70 and 25.9 nm for CeO_2-D, CeO_2-P, CeO_2-HL and CeO_2-HH, respectively. Moreover, the hydrothermally prepared samples display a broader PSD as compared to CeO_2-D and CeO_2-P samples.

The XRD patterns of the ceria samples are presented in Fig. 3. All samples exhibit similar patterns. The main peaks can be indexed to (111), (200), (220), (311), (222), (400), (331) and (420) planes of a face-centered cubic fluorite structure of ceria ($Fm3m$ symmetry, no. 225).[44] It is obvious that the samples CeO_2-HL and CeO_2-D have broader peaks than the other two samples, indicating a smaller crystallite size, D_{XRD}[16] (Table 1).
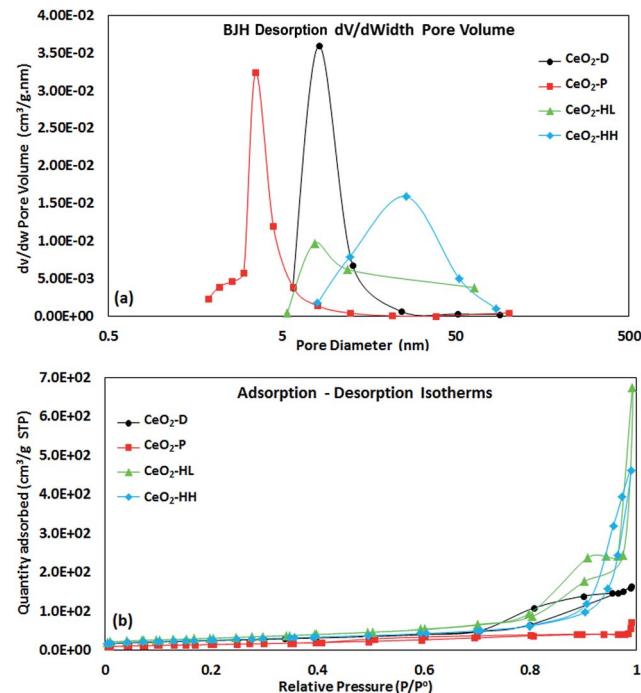

Fig. 2 BJH desorption pore size distribution (a) and adsorption–desorption isotherms (b) of as-prepared CeO_2 samples.

Redox properties (H_2-TPR)

TPR experiments were also carried out to investigate the impact of the preparation method on the redox properties of ceria samples. Fig. 4 presents the reduction profiles of the CeO_2 samples, which consist of two broad peaks centred at *ca.* 550 °C and 800 °C. They have been ascribed to the reduction of surface oxygen (O_s) and bulk oxygen (O_b) of ceria, respectively.[16,31,34,38,45] The H_2 consumption which corresponds to surface oxygen and bulk oxygen reduction is presented in Table 2. Notably, the ratio of O_s/O_b is affected by the preparation method, being higher for the samples prepared by the hydrothermal method. In particular, the following order, in terms of O_s/O_b ratio, is obtained: CeO_2-P (0.56) < CeO_2-D (0.72) < CeO_2-HL (0.94) < CeO_2-HH (1.13).
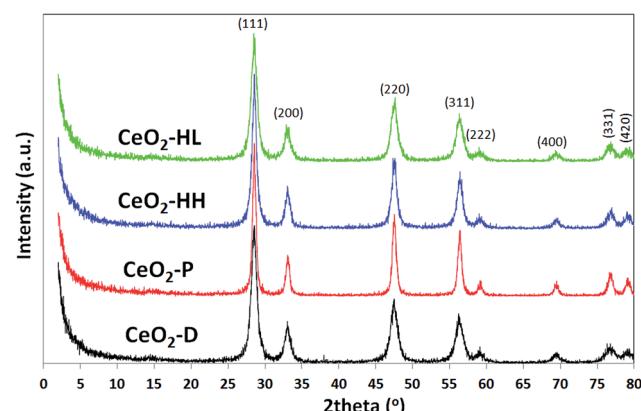
Fig. 3 XRD patterns of the CeO_2 samples.
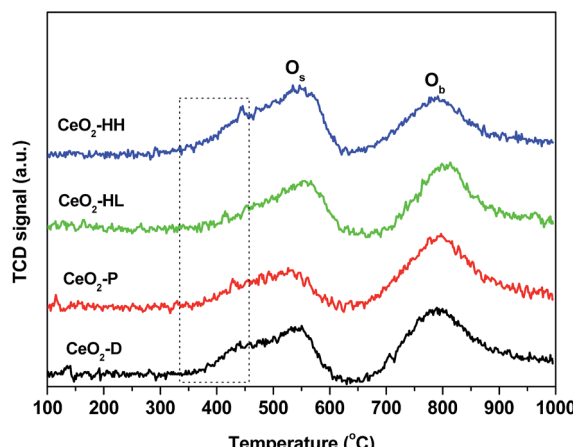
Fig. 4 H$_2$-TPR profiles of the CeO$_2$ samples.

Table 2 Redox characteristics of ceria samples

	H$_2$ consumption (mmol H$_2$ per g)			
Sample	O$_s$ peak	O$_b$ peak	Total	O$_s$/O$_b$ ratio
CeO$_2$-P	0.39	0.69	1.08	0.56
CeO$_2$-D	0.50	0.69	1.19	0.72
CeO$_2$-HL	0.48	0.51	0.99	0.94
CeO$_2$-HH	0.59	0.52	1.11	1.13

A closer inspection of the reduction profiles shows that the low temperature feature, attributed to surface oxygen reduction, consists of a main reduction peak at *ca.* 550 °C and a shoulder at *ca.* 440 °C, the latter being more evident for CeO$_2$-HH and CeO$_2$-D samples. However, the temperature of maximum H$_2$ consumption (T_{max}) is strongly dependent on exposed facets, being lower on {100} and {110} surfaces;[34,46] this probably indicates a higher contribution of these particular facets on CeO$_2$-HH and CeO$_2$-D samples. The latter is in agreement with the TEM analysis (Fig. 7), which implies the formation of nanorods over ceria-HH sample and in a lesser extent over CeO$_2$-D. In a similar manner, a decrease in the T_{max} by more than 100 °C has been observed with nanoshaped (nanocubes/nanorods) compared to polycrystalline conventional ceria.[34] Moreover, it should be noted that the size of CeO$_2$ NPs strongly affects the surface reduction, being facilitated at smaller sizes.[38] In view of the above aspects, the variation of surface-to-bulk oxygen, both in quantitative and qualitative terms (Fig. 4, Table 2), can be attributed to the different exposed facets as well as to the different size of ceria NPs.

The present findings unambiguously revealed the pronounced impact of hydrothermal synthesis on the reduction of surface-capping oxygen of ceria. The sample prepared by the hydrothermal method of high NaOH concentration (CeO$_2$-HH) shows the highest O$_s$/O$_b$ ratio, which is related to its improved reducibility and high oxygen mobility.[47]

Surface analysis (XPS)

Information about the different elements existing on the surface and their oxidation state are next obtained by X-ray photoelectron spectroscopy. High resolution spectra of Ce 3d and O 1s photoelectrons were obtained (Fig. 5a and b). The Ce 3d spectra are analyzed into eight components which correspond to four pairs of spin–orbit doublets (Fig. 5a).

The Ce 3d$_{3/2}$ and Ce 3d$_{5/2}$ spin–orbit components are labelled as u and v, respectively. The peaks labelled as v (882.4 eV), v″ (888.9 eV) and v‴ (898.3 eV) correspond to 3d$_{5/2}$ level of Ce^{4+}, while the peaks labelled as u (900.9 eV), u″ (907.7 eV) and u‴ (916.8 eV) are assigned to 3d$_{3/2}$ level of Ce^{4+}.[46] The v and v″

peaks are assigned to a mixing of Ce 3d^{9}4f^2 O 2p^4 and Ce 3d^{9}4f^1 O 2p^5 of Ce^{4+} states and the v‴ peak corresponds to the Ce 3d^{9}4f^0 O 2p^6 of Ce^{4+} final state.[48] The peaks tagged as v′ (883.7 eV) and u′ (902.2 eV) correspond to one of the two possible electron configurations of the final state of Ce^{3+} species. The ratio of the area for Ce^{3+} peaks to the whole peak area in Ce 3d region can lead to the relative amount of Ce^{3+}.[49] Table 3 shows that all samples have a similar amount of Ce^{3+}, which varies between 24.3 and 26.5%. These findings are in accordance with relative literature studies,[21,25] where it was found that very
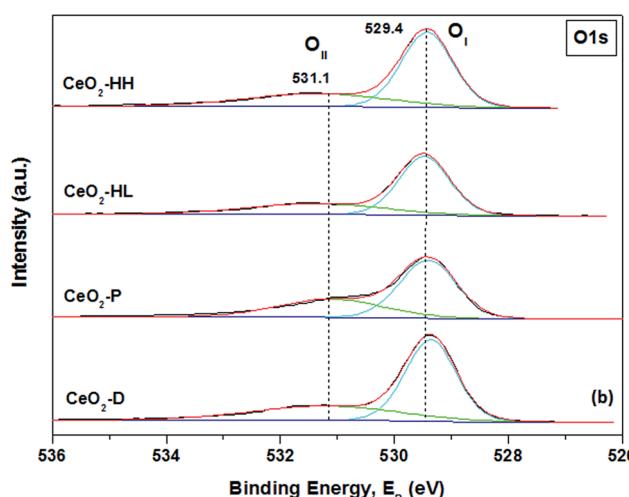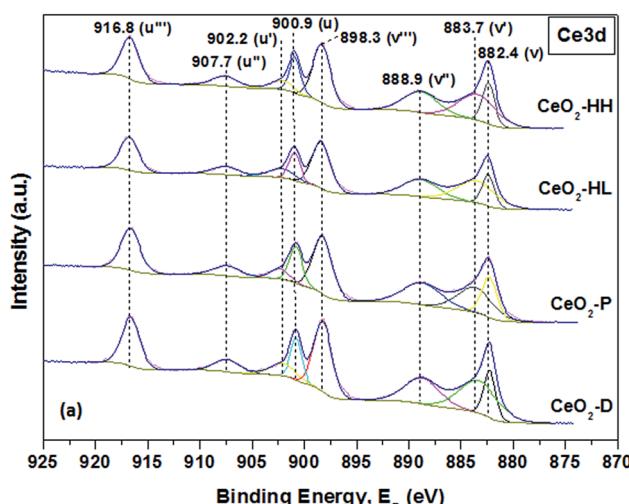

Fig. 5 XPS spectra of Ce 3d (a) and O 1s (b) region of CeO$_2$ samples.

similar Ce 3d spectra profiles can be obtained between ceria samples of different morphology, despite the quite different amount of defect sites in the subsurface/bulk of ceria. In any case, no definitive conclusions in relation to the contribution of Ce^{3+} on the different reducibility of the present samples can be revealed. In complete agreement, it was found that the concentration of Ce^{3+} species is almost the same among ceria NPs of different particle size, despite their extremely different redox characteristics.[38]

The corresponding O 1s spectra are illustrated in Fig. 5b. Curve-fitting reveals the presence of two peaks. The low binding energy peaks centred at 529.4 eV (O_I) are assigned to lattice oxygen while the peaks at 531.1 eV (O_{II}) are attributed to surface adsorbed oxygen species, hydroxyl/carbonate groups and oxygen vacancies.[49–52] The relative population of O_I and O_{II} along with their ratio (O_I/O_{II}) are included in Table 3. The CeO_2-HH sample exhibits the highest ratio (2.13), followed by CeO_2-HL (2.04), CeO_2-D (1.97) and CeO_2-P (1.71). Similar results in relation to the abundance of oxygen lattice (O_I) species on hydrothermally prepared ceria polymorphs have been recently reported.[53]

These findings in conjunction to the TPR results (*vide supra*) clearly demonstrated that CeO_2-HH sample have the highest population of loosely bound oxygen species, offering an improved reducibility and oxygen mobility. The latter is expected to notably affect the redox type mechanism involved in CO oxidation (*vide infra*).

Morphological characterization (SEM/TEM)

The SEM images of the ceria samples prepared by different methods are depicted in Fig. 6. Apparently, the samples exhibit different morphologies. CeO_2-D (Fig. 6a and b) shows different structures: large smooth flat surfaces along with smaller agglomerated particles (Fig. 6a). In some areas, the flat surfaces show some cracks, which resemble "star" forms (Fig. 6b). Nevertheless, EDS (not shown) performed in the different zones marked as Z1 and Z2 in Fig. 6a, showed that the composition is similar in all regions, including in Fig. 6b, that is, cerium oxide. CeO_2-P is shown in Fig. 6c and d and again different areas are seen, namely more "solid rocks" together with fragmented material. The sample prepared by the hydrothermal method employing high concentration of NaOH (Fig. 6g and h) implies the existence of a rod-like morphology whereas the hydrothermally prepared sample of low NaOH concentration (Fig. 6e and f) exhibits slight agglomeration of the NPs.

To clearly gain insight into the impact of preparation procedure on the morphological characteristics of ceria NPs, transmission electron microscopy (TEM) studies were also
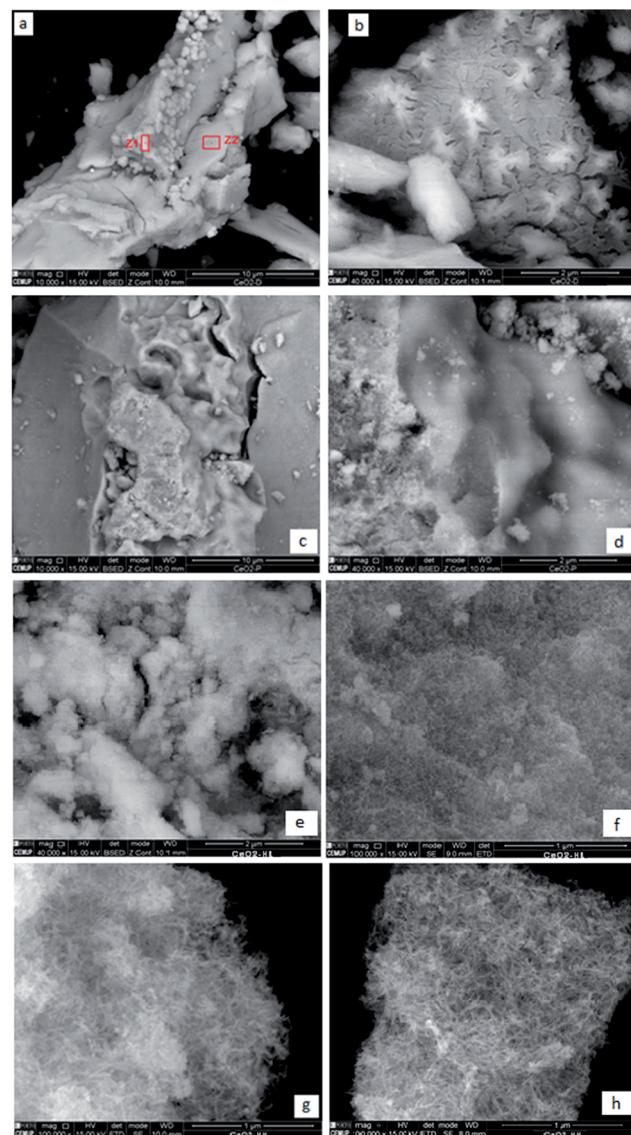

Fig. 6 SEM images of the samples: (a) and (b) CeO_2-D, (c) and (d) CeO_2-P, (e) and (f) CeO_2-HL, (g) and (h) CeO_2-HH.

carried out. Fig. 7 depicts representative images of the ceria samples. CeO_2-D (Fig. 7a and b) shows some needle like features with sizes up to 150 nm, and some smaller particles. CeO_2-P is shown in Fig. 7c and d and some spherical/polyhedral forms can be visualized ranging from 10–50 nm. The hydrothermally prepared sample of low NaOH concentration (Fig. 7e and f) exhibits mostly nanopolyhedra of irregular shapes, along with some nanorods. The sample prepared by the hydrothermal method employing high concentration of NaOH (Fig. 7g and h) shows the existence of a rod-like morphology, confirming the SEM results. The rods length varies from 25–200 nm.

Catalytic evaluation studies

The CO oxidation reaction was employed as a model reaction to gain insight into the extent of which the different synthesis method, and in turn the different physicochemical
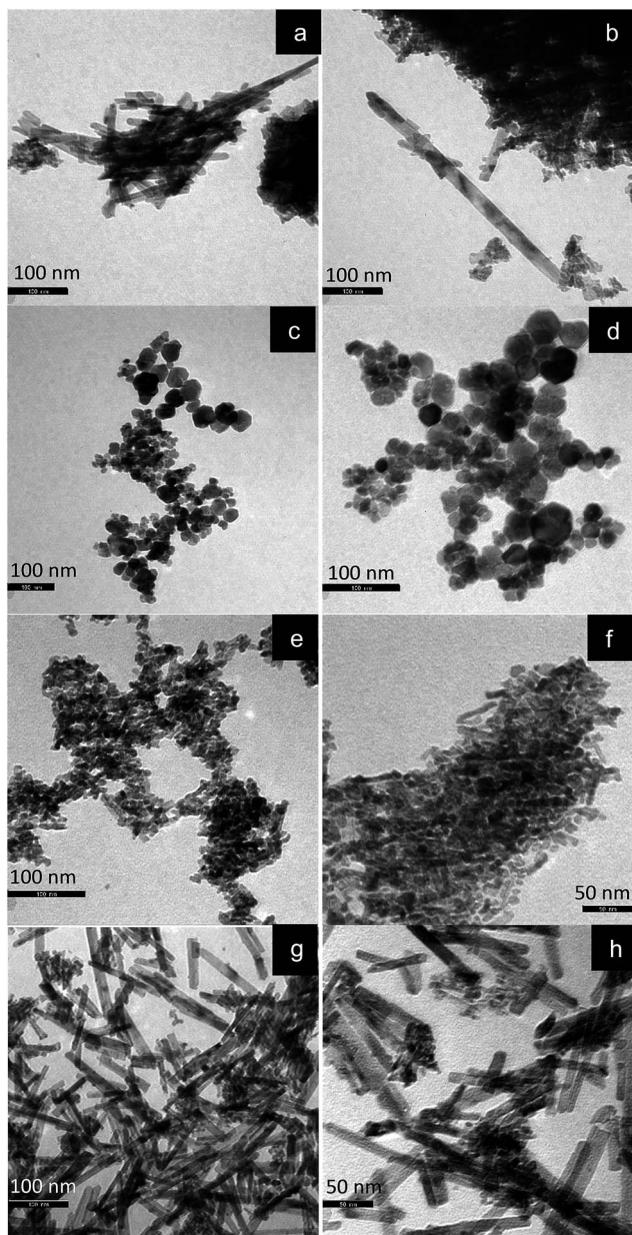
Table 3 XPS results for ceria samples

Sample	O_I (%)	O_{II} (%)	O_I/O_{II}	Ce^{3+} (%)
CeO_2-P	63.1	36.9	1.71	26.5
CeO_2-D	66.4	33.6	1.97	26.4
CeO_2-HL	67.1	32.9	2.04	25.3
CeO_2-HH	68.1	31.9	2.13	24.3

Fig. 7 TEM images of the samples: (a) and (b) CeO_2-D, (c) and (d) CeO_2-P, (e) and (f) CeO_2-HL, (g) and (h) CeO_2-HH.


Fig. 8 CO conversion as a function of temperature (a) and the corresponding Arrhenius plots (b) for CeO_2 samples.

characteristics (surface area, crystallite size, reducibility, surface oxygen, exposed facets), can affect the catalytic performance. Fig. 8a depicts the CO conversion as a function of temperature of the as-synthesized ceria samples. For comparison purposes, a commercial CeO_2 sample (Fluka) was employed as reference material. The superiority of the as-prepared samples as compared to the commercial one is evident. Moreover, the sample prepared by the hydrothermal method of high NaOH concentration (CeO_2-HH) demonstrated the optimum performance. In particular, the following oxidation performance, in terms of half-conversion temperature (T_{50}), was obtained: CeO_2-HH (320 °C) < CeO_2-HL (350 °C) < CeO_2-D (360 °C) < CeO_2-P (370 °C) < CeO_2-comm (460 °C).

The impact of synthesis procedure on the intrinsic reactivity can be more accurately obtained by the Arrhenius plots, in the kinetic regime (Fig. 8b). To take into account the differences in the BET surface area, the surface-normalized reaction rate (nmol m^{-2} s^{-1}) instead of CO conversion was employed. Table 4 summarizes the apparent activation energies (E_a) and the corresponding pre-exponential factors (A) for the ceria samples. The significant effect of synthesis method on the CO oxidation activity on the whole temperature range investigated is evident. The superiority of CeO_2-HH is again obvious, showing a specific reaction rate of about one order of magnitude higher, compared to other samples. Moreover, the calculated E_a for the CeO_2-HH sample is 43.7 kJ mol^{-1}, which is the lowest amongst the

Table 4 Kinetics parameters obtained by Arrhenius equation

Sample	Activation energy, E_a (kJ mol^{-1})	Pre-exponential factor, A (nmol s^{-1} m^{-2})
CeO_2-P	58.8	8.3×10^5
CeO_2-D	57.5	4.6×10^5
CeO_2-HL	53.8	2.5×10^5
CeO_2-HH	43.7	6.2×10^4

samples. In specific, the following order, in terms of E_a, was observed: CeO_2-HH (43.7 kJ mol^{-1}) < CeO_2-HL (53.8 kJ mol^{-1}) < CeO_2-D (57.5 kJ mol^{-1}) < CeO_2-P (58.8 kJ mol^{-1}), which is perfectly matched to conversion performance (Fig. 8a).

Based on the above, it can be stated that ceria NPs prepared by the hydrothermal method of high NaOH concentration (CeO_2-HH) showed the best catalytic performance for CO oxidation reaction, among all samples prepared in the present work. These findings can be interpreted on the basis of the well-established Mars-van Krevelen mechanism, in which ceria is reduced by CO and oxidized by gas phase oxygen through a redox cycle.

The main steps of this procedure are: (i) adsorption of CO on the ceria surface, (ii) reaction of the adsorbed CO with the lattice oxygen and formation of reaction intermediates, (iii) desorption of these intermediates and production of CO_2 and oxygen vacancies, (iv) replenishment of the oxygen vacancies by activating the gas phase oxygen on the catalyst.[30,48]

Since the above mechanistic steps exhibit a clear redox character, a strong dependence of CO oxidation performance from the redox properties of catalyst surface is expected. Indeed, the highly active CeO_2-HH sample demonstrated the highest population of loosely bound, easily reduced, surface oxygen species, resulting in the highest surface-to-bulk (O_s/O_b) oxygen species abundance (Table 2).

In view of this fact, a perfect trend between the half-conversion temperature (T_{50}) and the O_s/O_b ratio was revealed (Fig. 9), justifying the above argument. It is also of worth mentioning that although the CO oxidation performance was in general favoured by the surface area (Table 1), it seems not to be the decisive factor governing the CO oxidation activity. For instance, the CeO_2-HL sample possesses the highest surface area (109.4 m^2 g^{-1}), without, however, offering the best catalytic performance.

In summary, it can be inferred that the hydrothermal method of high NaOH concentration can result to the formation of CeO_2 NPs with rod-like morphology, with enhanced reducibility and surface oxygen exchange kinetics, and in turn CO oxidation activity.[30] The latter is schematically illustrated in Fig. 10, which depicts the impact of synthesis parameters on the solid state properties and consequently on the CO oxidation performance of ceria NPs, on the basis of the above described Mars-van Krevelen reaction model. The high concentration of loosely bound oxygen species on ceria nanorods, related to oxygen mobility and vacancies formation, can be accounted for the superior performance of the ceria-HH sample.

Hence, the O_s/O_b ratio, defined in the present work, can be considered as a reliable descriptor for the CO oxidation performance of ceria NPs. In view of this fact, in a comprehensive study by M. Capdevila-Cortada et al.,[46] exploring the reactivity descriptors for ceria-based materials, the surface reduction (E_{red}) and oxygen basicity (O_{2p})-linked to vacancy formation energy and the number of adsorption sites-can be considered as the most important reactivity descriptor. Hence, the CO oxidation rate is expected to follow the order $r_{110} > r_{100} > r_{111}$, in agreement with the vacancy formation energy.[46]

In light of the above, it has been clearly revealed, both theoretically[32,33] and experimentally[30,31,34] that anionic vacancies formation is strongly dependent on exposed facets of ceria, being lower on rod-like formations, where the {110} and {100} planes are prevailing. In a similar manner, the improved low temperature CO oxidation performance of various transition metals supported on CeO_2-nanorods has been ascribed to the pronounced effect of ceria nanorods towards the formation of oxygen vacancies and CO adsorption sites.[10] The key role of redox properties, and in particular of loosely bound oxygen species, on the CO oxidation performance was recently verified by Reddy and co-workers in a series of doped ceria samples.[48] A direct correlation between the lattice oxygen binding energy and the activity was revealed, implying that oxygen species migration from bulk to surface may determine the overall process. It should be noted, however, that no similar correlation has been
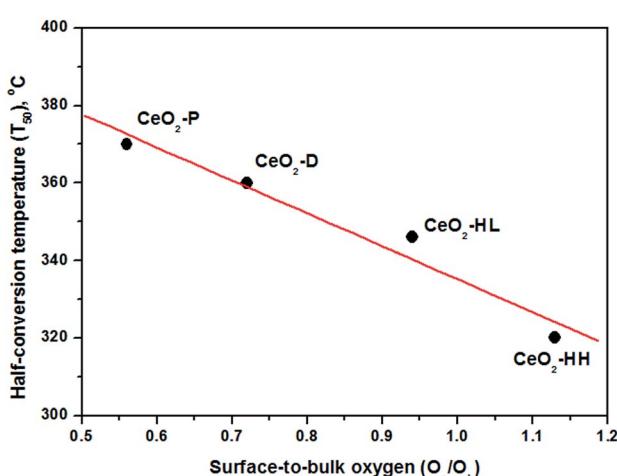

Fig. 9 Correlation between the half-conversion temperature (T_{50}) and the O_s/O_b TPR ratio.
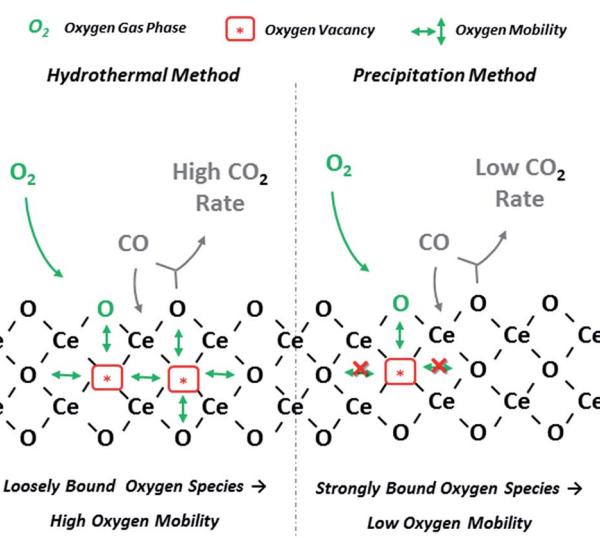

Fig. 10 Schematic illustration of CO oxidation mechanism on CeO_2 NPs prepared by different methods.

observed in the present work; the lattice oxygen binding energy of bare ceria samples is not strongly affected by the preparation method (Fig. 5). Instead of that, a direct correlation between the catalytic performance and the abundance of easily reduced (weakly bound) oxygen species is observed (Fig. 9).

Taking into account the superior reducibility of CeO_2-HH sample, it would be of particular importance to explore the solid state properties and the catalytic performance of binary metal/CeO_2-HH composites. The enhanced redox properties of ceria carrier are expected to notably affect the extent of metal-support interactions[15,54,55] and in turn the catalytic activity.

Conclusions

The impact of synthesis parameters on the solid state properties of CeO_2 materials was investigated. CeO_2 prepared by hydrothermal method of high NaOH concentration (CeO_2-HH) demonstrated the optimum CO oxidation performance, with the lowest E_a (43.7 kJ mol^{-1}) amongst the other ceria samples prepared by precipitation, decomposition and hydrothermal with low NaOH concentration. Interestingly, the CO conversion performance of CeO_2-HH sample outperforms notably that of commercial sample, lowering by ca. 150 °C the half-conversion temperature (T_{50}). A direct quantitative correlation between the catalytic performance and the abundance of weakly bound (easily reduced) oxygen species was revealed. The rod-like morphology of CeO_2-HH nanoparticles, with well-defined {100} and {110} reactive planes, favours the enhanced reducibility and lattice oxygen mobility, rendering this material appropriate as catalyst or supporting carrier.

Acknowledgements

References

1 T. Montini, M. Melchionna, M. Monai and P. Fornasiero, *Chem. Rev.*, 2016, **116**, 5987–6041.

2 W.-X. Tang and P.-X. Gao, *MRS Commun.*, 2016, **6**, 311–329.

3 D. Zhang, X. Du, L. Shi and R. Gao, *Dalton Trans.*, 2012, **41**, 14455–14475.

4 Z. L. Wang, G. R. Li, Y. N. Ou, Z. P. Feng, D. L. Qu and Y. X. Tong, *J. Phys. Chem. C*, 2011, **115**, 351–356.

5 Z. X. Ji, X. Wang, H. Y. Zhang, S. J. Lin, H. Meng, B. B. Sun, S. George, T. Xia, A. E. Nel and J. I. Zink, *ACS Nano*, 2012, **6**, 5366–5380.

6 Y. Kang, M. Sun and A. Li, *Catal. Lett.*, 2012, **142**, 1498–1504.

7 J. Han, H. J. Kim, S. Yoon and H. Lee, *J. Mol. Catal. A: Chem.*, 2011, **335**, 82–88.

8 M. Nolan, in *Catalysis by materials with well-defined structures*, ed. Z. Wu and S. H. Overbury, Elsevier Science, USA, 2015, ch. 6, pp. 159–192.

9 M. Melchionna and P. Fornasiero, *Mater. Today*, 2014, **17**(7), 349–357.

10 S. A. Mock, S. E. Sharp, T. R. Stoner, M. J. Radetic, E. T. Zell and R. Wang, *J. Colloid Interface Sci.*, 2016, **466**, 261–267.

11 S. W. Yu, H. H. Huang, C. W. Tang and C. B. Wang, *Int. J. Hydrogen Energy*, 2014, **39**(35), 20700–20711.

12 L. Soler, A. Casanovas, A. Urrich, I. Angurell and J. Llorca, *Appl. Catal., B*, 2016, **197**, 47–55.

13 M. Piumetti, S. Bensaid, N. Russon and D. Fino, *Appl. Catal., B*, 2015, **165**, 742–751.

14 C. P. Vinod, *Catal. Today*, 2010, **154**(1–2), 113–117.

15 M. Konsolakis, *Appl. Catal., B*, 2016, **198**, 49–66.

16 J. Liu, Z. Zhao, J. Wang, C. Xu, A. Duan, G. Jiang and Q. Yang, *Appl. Catal., B*, 2008, **84**(1–2), 185–195.

17 A. I. Y. Tok, F. Y. C. Boey, Z. Dong and X. L. Sun, *J. Mater. Process. Technol.*, 2007, **190**(1–3), 217–222.

18 I. Ilgaz Soykal, H. Sohn, J. T. Miller and U. S. Ozkan, *Top. Catal.*, 2014, **57**(6–9), 785–795.

19 L. Yin, Y. Wang, G. Pang, Y. Koltypin and A. Gedanken, *J. Colloid Interface Sci.*, 2002, **246**(1), 78–84.

20 F. Gu, Z. Wang, D. Han, C. Shi and G. Guo, *Mater. Sci. Eng., B*, 2007, **139**(1), 62–68.

21 M. Piumetti, T. Andana, S. Bensaid, N. Russo, D. Fino and R. Pirone, *Nanoscale Res. Lett.*, 2016, **11**, 165.

22 X. Lu, D. Zheng, J. Gan, Z. Liu, C. Liang, P. Liu and Y. Tong, *J. Mater. Chem.*, 2010, **20**, 7118–7122.

23 M. Kovacevic, B. L. Mojet, J. G. Van Ommen and L. Lefferts, *Catal. Lett.*, 2016, **146**(4), 770–777.

24 J. M. López, A. L. Gilbank, T. García, B. Solsona, S. Agouram and L. Torrente-Murciano, *Appl. Catal., B*, 2015, **174–175**, 403–412.

25 Z. Wu, M. Li, J. Howe, H. M. Meyer III and S. H. Overbury, *Langmuir*, 2010, **26**(21), 16595–16606.

26 H. He, P. Yang, J. Li, R. Shi, L. Chen, A. Zhang and Y. Zhu, *Ceram. Int.*, 2016, **42**(6), 7810–7818.

27 J. Liu, Y. Li, J. Zhang and D. He, *Appl. Catal., A*, 2016, **513**, 9–18.

28 Y. Makinose, T. Taniguchi, K. I. Katsumata, K. Okada and N. Matsushita, *Adv. Powder Technol.*, 2016, **27**(1), 64–71.

29 R. Rao, M. Yang, C. Li, H. Dong, S. Fang and A. Zhang, *J. Mater. Chem. A*, 2015, **3**, 782–788.

30 Z. Wu, M. Li and S. H. Overbury, *J. Catal.*, 2012, **285**, 61–73.

31 G. Vilé, S. Colussi, F. Krumeich, A. Trovarelli and J. Pérez-Ramírez, *Angew. Chem., Int. Ed.*, 2014, **53**, 12069–12072.

32 M. Nolan, S. C. Parker and G. W. Watson, *Surf. Sci.*, 2005, **595**(1–3), 223–232.

33 M. Nolan, J. E. Fearon and G. W. Watson, *Solid State Ionics*, 2006, **177**(35–36), 3069–3074.

34 E. Aneggi, D. Wiater, C. De Leitenburg, J. Llorca and A. Trovarelli, *ACS Catal.*, 2014, **4**, 172–181.

35 M. Piumetti, B. van der Linden, M. Makkee, P. Miceli, D. Fino, N. Russo and S. Bensaid, *Appl. Catal., B*, 2016, **199**, 96–107.

36 S. Saitzek, J.-F. Blach, S. Villain and J.-R. Gavarri, *Phys. Status Solidi A*, 2008, **205**(7), 1534–1539.

37 R. Barthos, A. Hegyessy, S. Klébert and J. Valyon, *Microporous Mesoporous Mater.*, 2015, **207**, 1–8.

38 J. Xu, J. Harmer, G. Li, T. Chapman, P. Collier, S. Longworth and S. C. Tsang, *Chem. Commun.*, 2010, **46**, 1887–1889.

39 R. Dziembaj, M. M. Zaitz, M. Rutkowska, M. Molenda and L. Chmielarz, *Catal. Today*, 2012, **191**(1), 121–124.

40 L. M. Walter and J. W. Morse, *J. Sediment. Res.*, 1984, **54**(4), 1081–1090.

41 Y.-P. Fu, S.-B. Wen and C.-H. Lu, *Progress in Nanotechnology: Applications*, The American Ceramics Society, John Wiley & Sons, 2010, pp. 197–203.

42 A. Teleki, R. Wengeler, L. Wengeler, H. Nirschl and S. E. Pratsinis, *Powder Technol.*, 2008, **181**(3), 292–300.

43 A. B. Noor, M. Asri and B. Mohd, *J. Phys. Sci.*, 2008, **19**(2), 93–104.

44 M. Farahmandjou and M. Zarinkamar, *Journal of Ultrafine Grained and Nanostructured Materials*, 2015, **48**(1), 5–10.

45 J.-Y. Luo, M. Meng, X. Li, X.-G. Li, Y.-Q. Zha, T.-D. Hu, Y.-N. Xie and J. Zhang, *J. Catal.*, 2008, **254**(2), 310–324.

46 M. Capdevila-Cortada, G. Vilé, D. Teschner, J. Pérez-Ramírez and N. López, *Appl. Catal., B*, 2016, **197**, 299–312.

47 Z. Hu, X. Liu, D. Meng, Y. Guo, Y. Guo and G. Lu, *ACS Catal.*, 2016, **6**(4), 2265–2279.

48 D. Mukherjee, B. G. Rao and B. M. Reddy, *Appl. Catal., B*, 2016, **197**, 105–115.

49 H. Jin, R. You, S. Zhou, K. Ma, M. Meng, L. Zheng, J. Zhang and T. Hu, *Int. J. Hydrogen Energy*, 2015, **40**(10), 3919–3931.

50 M. Konsolakis, Z. Ioakimidis, T. Kraia and G. Marnellos, *Catalysts*, 2016, **6**(3), 39.

51 S. A. C. Carabineiro, M. Konsolakis, G. E. N. Marnellos, M. F. Asad, O. S. G. P. Soares, P. B. Tavares, M. F. R. Pereira, J. J. De Melo Órfão and J. L. Figueiredo, *Molecules*, 2016, **21**, 644.

52 L. Soler, A. Casanovas, C. Escudero, V. Pérez-Dieste, E. Aneggi, A. Trovarelli and J. Llorca, *ChemCatChem*, 2016, **8**, 1–5.

53 G. Li, B. Wu and L. Li, *J. Mol. Catal. A: Chem.*, 2016, **424**, 304–310.

54 G. N. Vayssilov, Y. Lykhach, A. Migani, T. Staudt, G. P. Petrova, N. Tsud, T. Skála, A. Bruix, F. Illas, K. C. Prince, V. Matolín, K. M. Neyman and J. Libuda, *Nat. Mater.*, 2011, **10**, 310–315.

55 D. R. Mullins and K. Z. Zhang, *Surf. Sci.*, 2002, **513**, 163–173.